Pure Appl. Geophys. 177 (2020), 1335–1346

https://doi.org/10.1007/s00024-020-02433-z

Pure and Applied Geophysics

A Multi-fault Model Estimation from Tsunami Data: An Application to the 2018 M7.9 Kodiak Earthquake

M. Jakir Hossen,[1] Anne F. Sheehan,[2] and Kenji Satake[3]

Abstract—In this study, we developed a new search algorithm to find a multi-fault model of a complex earthquake using tsunami data, and applied it to the January 23, 2018 M7.9 Kodiak earthquake. Our method includes a Green’s function based time reverse imaging (GFTRI) approach to invert for sea surface displacement using tsunami waveforms, followed by inversion of the sea surface displacement for the earthquake slip distribution. The global CMT focal mechanism for this event indicates that faulting occurred on a steeply dipping fault striking either N–S (right lateral) or E–W (left lateral), while subsequent work reveals a more complex pattern of strike-slip faulting. We carried out a number of source inversions using different combinations of faults to find the model based on an extremum for residual errors. Our results suggest that the rupture occurred on at least three faults oriented in approximately N–S and E–W directions. We further explored the fault-geometry parameters by perturbing them within a range suggested by previous work. We found that the sea surface displacement model is best fit by our preferred three fault-model with the set of parameters (strike, dip, rake): (165°, 60°, 154°) and (265°, 60°, 10°) for N–S and E–W directions, respectively.

Keywords: Tsunami source inversion, multi-fault model, time reverse imaging.

1. *Introduction*

A large tsunami is usually generated by a megathrust earthquake, for example, the 1964 M 9.2 Great Alaska Earthquake, the 2011 M 9.1 Tohoku-Oki earthquake, or the 2004 M 9.1 Sumatra earthquake. Such earthquakes occur in subduction zones at the boundary of the continental plate over the oceanic plate, and displace a huge amount of water due to vertical movement of the sea-floor. However, intraplate events at outer-rise regions of the incoming plate can also generate destructive tsunamis. These earthquakes are typically strike-slip and are less likely to cause vertical deformation of the sea-floor and displace a large amount of water. A few outer-rise events have caused tsunamis in the past, for example, the 11 April 2012 M 8.2 Sumatra earthquake (Yue et al. 2012).

On January 23, 2018 at 9:31:42 UTC, an earthquake of M_w 7.9 occurred at 56.046° N, 149.073° W, 300 km southeast of Kodiak Island, Alaska. The event was on the incoming Pacific plate in the outer rise region of the Alaska-Aleutian subduction zone. The focal mechanism solutions indicate that faulting occurred on a steeply dipping fault either N–S striking (right lateral) or E–W striking (left lateral). According to the centroid moment tensor (CMT) solution of US Geological Survey (USGS), the seismic moment is $1.01 \times 10^{21} Nm$, Magnitude is $M_w = 7.9$ and the centroid depth is 32.0 km; the nodal planes have strike $\psi_1 = 261°$, dip $\phi_1 = 69°$, rake $r_1 = 18°$ and strike $\psi_2 = 164°$, dip $\phi_2 = 74°$, rake $r_2 = 158°$. This single fault-model for the event provides a reasonable fit to teleseismic body and surface waves but the aftershock seismicity shows a broad and complex spatial distribution. Recent studies suggest that the rupture might have occurred on several fault planes instead of a single fault (e.g, Ruppert et al. 2018; Lay et al. 2018; Zhao et al. 2018). Ruppert et al. (2018) used teleseismic P wave back-projection and GPS modeling to find their proposed model consisting of five ruptured

Electronic supplementary material The online version of this article (https://doi.org/10.1007/s00024-020-02433-z) contains supplementary material, which is available to authorized users.

---

[1] Cooperative Institute of Research in Environmental Sciences, University of Colorado, Boulder, CO, USA. E-mail: md.hossen@colorado.edu

[2] Department of Geological Sciences and Cooperative Institute of Research in Environmental Sciences, University of Colorado, Boulder, CO, USA.

[3] Earthquake Research Institute, The University of Tokyo, Tokyo, Japan.

Birkhäuser

subfaults, among which a NE–SW trending left-lateral strike slip segment released the most energy. Lay et al. (2018) suggested a four-fault model, dominated by right lateral slip on a westward-dipping fault, is most compatible with most seismic, GPS and tsunami data. Using onshore GPS data, Zhao et al. (2018) also proposed a four-fault model where the seismic moment is mainly released on two WSW oriented fault planes.

There are several ways to estimate tsunami source models using tsunami data, including least-squares (LSQ) (Satake 1987; Wei et al. 2003; Satake et al. 2013; Baba and Cummins 2005; Gusman et al. 2016; Mulia and Asano 2016; Hossen et al. 2015b; Ho et al. 2017), genetic algorithms (Mulia and Asano 2016), time reverse imaging (TRI) (Hossen et al. 2015c; An et al. 2014) and Green's function based time reverse imaging (GFTRI) methods (Hossen et al. 2015a). The GFTRI method involves convolution of a set of Green's functions (GFs) with the time-reversed observed tsunami waveforms. The method was applied successfully to the 2011 Tohoku-Oki megathrust earthquake tsunami and the 2009 Samoa earthquake tsunami (Hossen et al. 2018).

In this paper, we adopted a two-step inversion (TSI) for the 2018 Kodiak earthquake. In the first step, the GFTRI method is used to determine a sea surface displacement (SSD) model. In the second step, we determine the slip distribution of the earthquake from the sea surface displacement, inverting for slip distribution on the fault planes. The estimation of slip distribution from the SSD model is computationally efficient and does not require the user to recompute waveforms (tsunami and seismic)

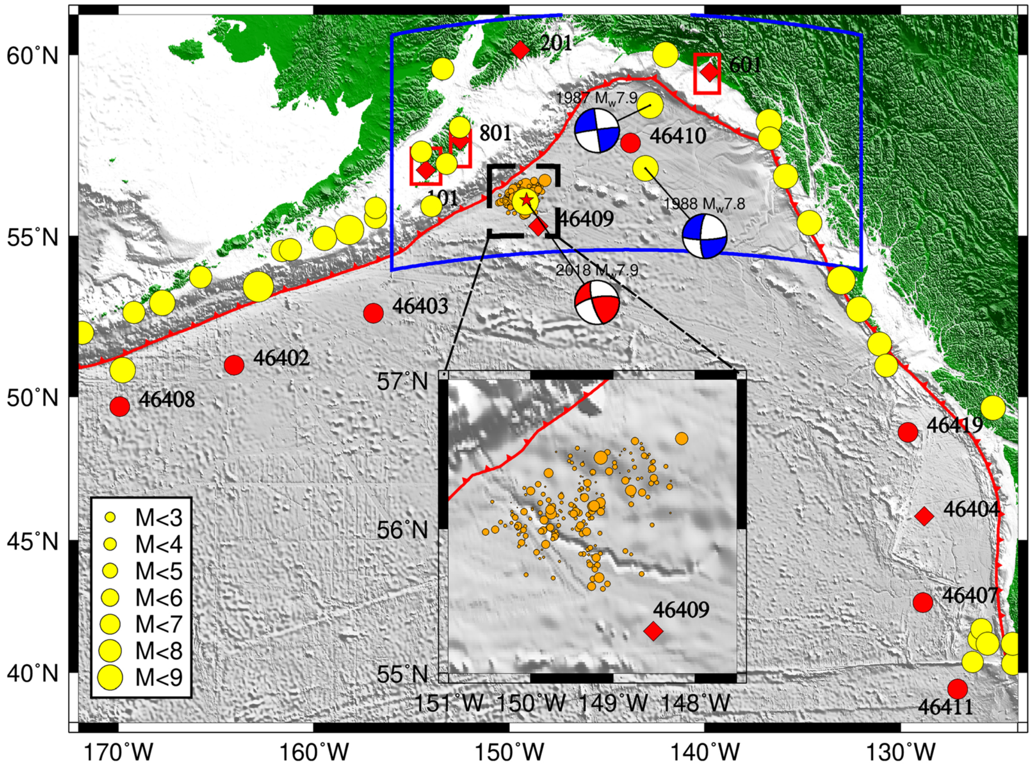

Figure 1

Map of study area, seismicity, and tsunami observing stations. Red star shows hypocenter of the January 23, 2018 M 7.9 offshore Kodiak earthquake. Inset map corresponds to dashed black box and shows aftershock distribution (orange circles) of the offshore Kodiak event. Focal mechanism for the 2018 Kodiak earthquake and two other outer rise earthquakes are also shown. Yellow circles show past earthquakes with $M_w > 5$. Tsunami observation stations are depicted by red circles and diamonds, with red circles used in the tsunami source estimation and all stations used in comparison of model to observations. For the tsunami modeling we used three nested domains with grid-spacing of 60 arc sec (for entire map area), 20 arc sec (blue box) and 20/3 arc sec (red boxes)

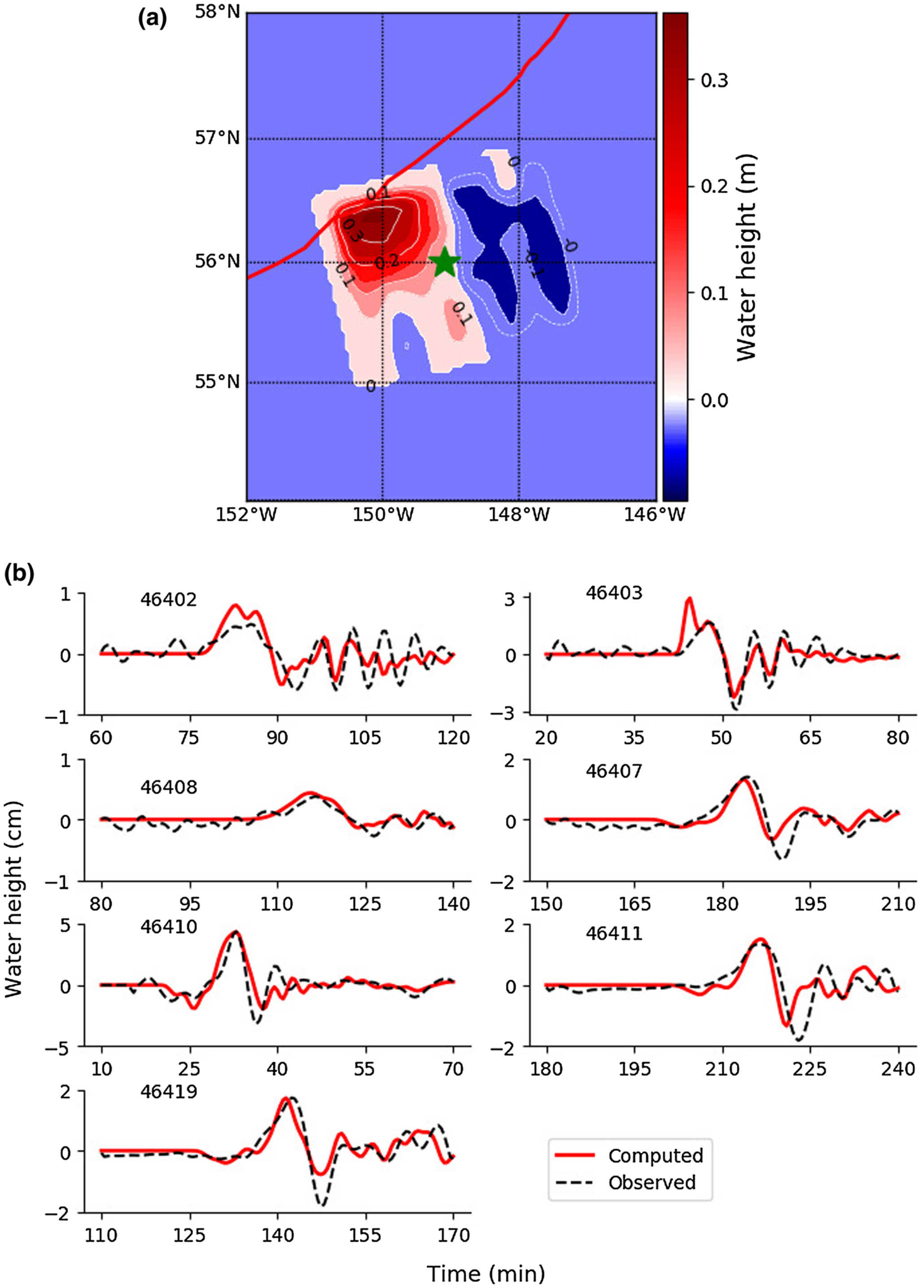

Figure 2

a The initial sea surface displacement model (SSD) for the 2018 offshore Kodiak tsunami obtained from Green's function based time reverse imaging (GFTRI) of tsunami waveform data from DART buoys 46402, 46403, 46407, 46408, 46410, 46411, and 46419. **b** Agreement between observed (dashed black) and computed tsunami waveforms (red) at DART buoys 46402, 46403, 46407, 46408, 46410, 46411, and 46419 as GFs, instead the sea-floor deformation computed by the Okada (1985) model for each sub-fault are used as GFs in the inversion. The TSI approach has been applied to several earthquake events, such as the 2017 Tehuantepec (Mexico) earthquake (Gusman et al. 2018) and the 2009 Samoa earthquake (Hossen et al. 2018) to characterize the earthquake faults.

2. Data

Thirteen DART and tide gauge stations in the NE Pacific with high quality recordings of the 2018 Kodiak earthquake and tsunami were utilized in our analysis (Figure 1, Table T1 in Supplement). DART sea-floor absolute pressure records for the 2018 Kodiak earthquake and tsunami were obtained from the National Oceanic and Atmospheric Administration-National Data Buoy Center (http://www.ndbc.noaa.gov/dart.shtml) (Mungov et al. 2013). Coastal tide gauge records were obtained from the Intergovernmental Oceanographic Commission-United Nations Educational, Scientific and Cultural Organization sea level monitoring (http://www.ioc-sealevelmonitoring.org/index.php). The tsunami waveforms are prepared by resampling, detiding and filtering. The sampling interval of the tide gauge is 60 s, while that of the DART is 15–60 s (event mode vs. continuous). For waveform data processing and inversion purposes, we resampled all of the tsunami time series data to 30 s time interval. For removing tides, we used a low sample rate of 15 min and removed the tidal component by estimating a polynomial fit and removing it from the records. After removing the tidal signal the data were bandpass filtered using a Butterworth filter with cutoff periods from 1.5 h (0.000185185 Hz) to 4 min (0.004166667 Hz).

3. Methodology

In the first step of our inversion, we estimate the SSD model by implementing the Green's function based time reverse imaging (GFTRI) method as described in Hossen et al. (2015a). The GFTRI method uses precomputed Green's functions (GFs) from a unit source to each observation station, convolves the GFs with the time reversed observed waveforms and then scales the reverse wave-field by the GFs to estimate amplitude over each source patch. The source patches are obtained by dividing the source domain; over each source patch a unit source is created by using a box function with cosine tapering. The dimension of each source patch is 25 × 25 km^2, which makes in total 60 source grid points (Supplementary Figure S1) for the 250 × 150 km^2 source area of the 2018 Kodiak Alaska tsunami. The GFTRI has the advantage that it does not require the use of the LSQ method to solve the evolved linear system and additionally does not need regularization constraints (Hossen et al. 2015a). However, the GFTRI method requires a tsunami propagation model to satisfy the reciprocity principle (Korolev 2011). To compute the GFs, we use the JAGURS tsunami propagation model that satisfies the reciprocity principle (see for details, Hossen et al. 2015c; Mulia et al. 2018). JAGURS solves the two dimensional nonlinear shallow water equations with Boussinesq dispersion in a finite difference scheme (Baba et al. 2017). This code is parallelized, hence reducing the computational time significantly.

Figure 3

▶

Residual errors obtained using different fault parameterizations in the earthquake slip inversion. **a** Case 1a, residual error for inversion with a single fault (F_1 to F_9) oriented in the N–S direction. **b** Case 1b, residual error for inversion with a single fault (S_1 to S_9) in the E–W direction. For Case 1 (single fault), fault F_4 provides the smallest residual error. **c** Case 2, fault F_4 plus one fault from the N–S direction is used in the inversion; **d** Case 3a, faults (F_4 & S_5) and an additional fault in the E–W direction; **e** Case 3b, faults (F_4 & S_5) and an additional fault in the N–S direction. The smallest error (**d**) is obtained with the set $\{F_4, F_8, S_5\}$. **f** Case 4, faults (F_4, F_8 & S_5) with one additional fault in the N–S direction. In this case (case 4), the improvement in fit (reduction of error) is very slight. In a similar fashion, we considered five and six faults in cases 5 & 6 and find that the error reduction (**g**, **h**) is very slight

We set our computational domain to latitude 38° N–61° N and longitude 172° W–124° W in order to cover the epicenter and the locations of the observation stations considered in this work (Fig. 1). We considered three nested grids in our simulation: the coarsest grid resolution (60 arc-sec) bathymetry derived from the General Bathymetry Chart of the Ocean global database (Weatherall et al. 2015) over

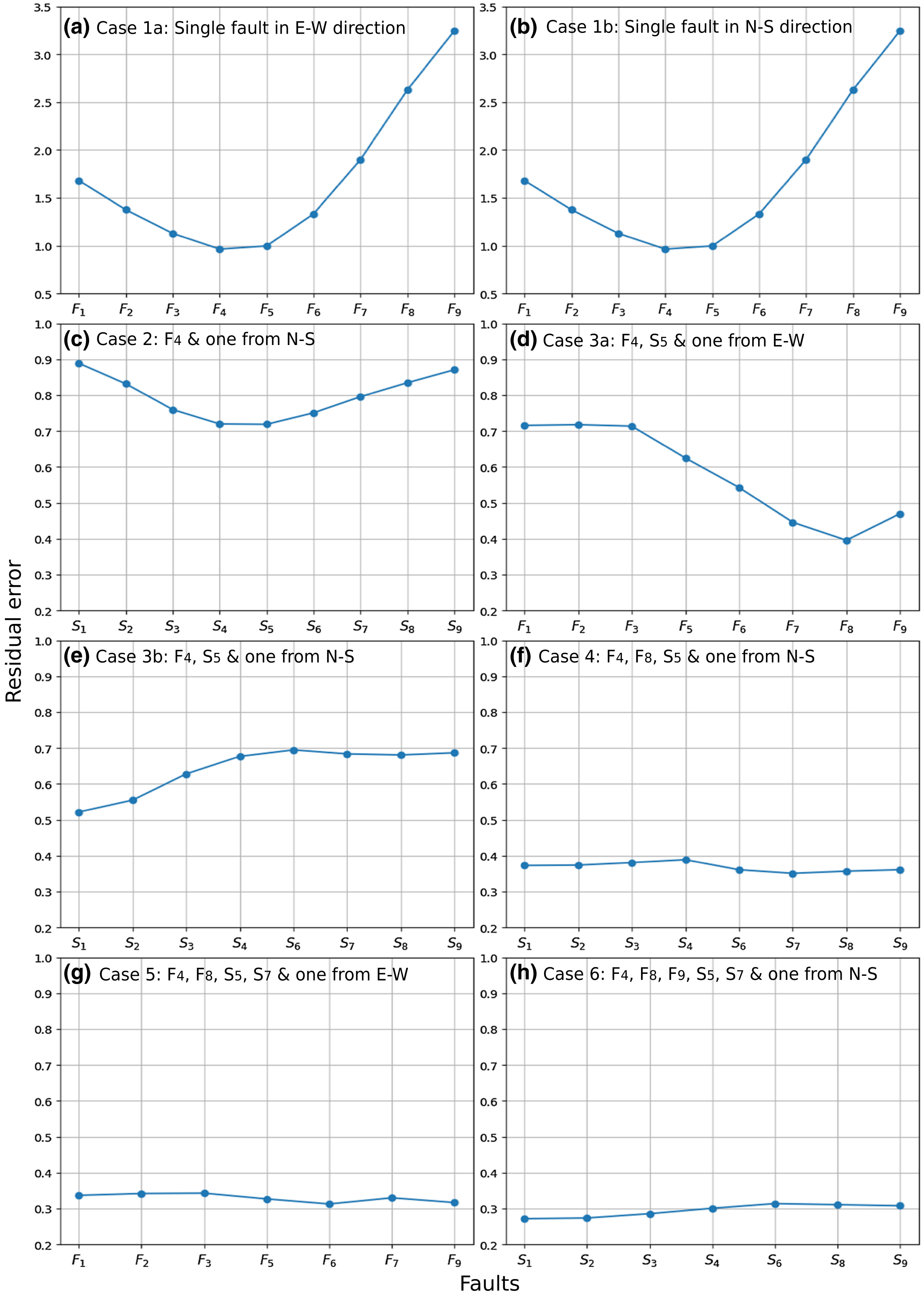
(a) Case 1a: Single fault in E-W direction
(b) Case 1b: Single fault in N-S direction
(c) Case 2: F4 & one from N-S
(d) Case 3a: F4, S5 & one from E-W
(e) Case 3b: F4, S5 & one from N-S
(f) Case 4: F4, F8, S5 & one from N-S
(g) Case 5: F4, F8, S5, S7 & one from E-W
(h) Case 6: F4, F8, F9, S5, S7 & one from N-S
Residual error
Faults
0.5
1.0
1.5
2.0
2.5
3.0
3.5
0.2
0.3
0.4
0.5
0.6
0.7
0.8
0.9
1.0
F_1 F_2 F_3 F_4 F_5 F_6 F_7 F_8 F_9
S_1 S_2 S_3 S_4 S_5 S_6 S_7 S_8 S_9
F_1 F_2 F_3 F_5 F_6 F_7 F_8 F_9
S_1 S_2 S_3 S_4 S_6 S_7 S_8 S_9
F_1 F_2 F_3 F_5 F_6 F_7 F_9
S_1 S_2 S_3 S_4 S_6 S_8 S_9

the entire domain, intermediate grid resolution (20 arc-sec) derived from the bathymetry provided by NOAA for the domain (54° N–60.5° N, 156° W–132° W) and the finest grid resolution (20/3 arc sec) derived from the same bathymetry for the domain shown in Fig. 1 (red boxes). The time step for this computation is set as 0.5 s.

In the second step of our inversion, we estimate the earthquake slip distribution by inverting the SSD model. From the earthquake slip distribution, we then compute a co-seismic water surface displacement (WSD) model which can be compared to the input SSD. We determine the slip distribution by solving a linear system $Gm = d$ using a least squares method with regularization constraints (damping and smoothing). The matrix G contains the sea-floor deformation from each sub-fault calculated by Okada (1985) elastic dislocation model and the vector d contains the SSD model as grid points (explained in detail in Sect. 5).

4. Sea Surface Displacement Model

The initial sea surface displacement (SSD) model that we determine using GFTRI is shown in Fig. 2a. In this source analysis, we use seven DART buoys (46402, 46403, 46407, 46408, 46410, 46411, 46419) located in the deep ocean surrounding the earthquake source. These stations are selected because the quality of recordings is excellent, the bathymetry data surrounding these stations is more accurate than at shallow sites and grid resolution near these stations does not have a significant impact on GFs. We consider only 1 h of data after the first arrival of tsunami in order to avoid coastal reflection or local resonance. We do not use DART 46409 because it is too close to the source for reciprocity to hold (Hossen et al. 2015a).

In GFTRI method, the amplitude of each unit source is calculated by

$$a_i = \frac{1}{p}\sum_{j=1}^{p}\frac{1}{|G_{ij}|^2}TR_j(s_i, T-\delta t_i), \qquad (1)$$

where δt_i is the time adjustment (for details, see Hossen et al. (2015a)), p is the number of stations, T is the time length and $TR_j(s_i, \cdot)$ is the reverse wavefield obtained by convolving GFs from the ith source with the jth observation in reverse time order. In this study, we find that time adjustment does not provide a reliable SSD model that fits observed waveforms well. Instead, it is important to include an attenuation factor γ to account for decrease in tsunami height with propagation away from the source. Thus, the equation for calculating the amplitude becomes

$$a_i = \frac{1}{p}\sum_{j=1}^{p}\frac{1}{\gamma|G_{ij}|^2}TR_j(s_i, T)\,. \qquad (2)$$

We find that an attenuation factor of 2 determined by trial and error basis provides a more accurate SSD model than a model with time adjustment. The resulting agreement between observed and simulated waveforms is very good at most of the stations, the period of the waveforms matches very well, and the peak amplitude is close to that observed (Fig. 2b). The resulting displaced surface water model is mostly concentrated between the trench line and the epicenter, with maximum water height of approximately 30 cm (Fig. 2a).

5. Fault Slip Distribution

In the second step of the inversion, we estimate the earthquake slip distribution from the SSD model. The aftershock distribution of the Kodiak event suggests that the rupture likely occurred on both N–S and E–W trending faults, and subsequent studies indicate that the rupture likely took place on a complex distribution of multiple fault planes oriented in the N–S and E–W directions (e.g, Lay et al. 2018; Ruppert et al. 2018; Krabbenhoeft et al. 2018; Zhao et al. 2018). We use the SSD model to find the

Figure 4 ▶
a A schematic diagram of the fault planes considered in the earthquake slip distribution estimation. Fault planes in the N–S direction (purple) have strike 164° and planes in the E–W direction (yellow) have strike 261°. **b**, **c** The fault models for case 1 (one fault in each direction is identified as the ruptured fault); **d** slip distribution for case 2, which has two faults (F_4 and S_5) and **e** slip distribution for case 3, with 3 faults (F_4, F_8 and S_5). Case 3 is our preferred fault model for the 2018 Kodiak earthquake

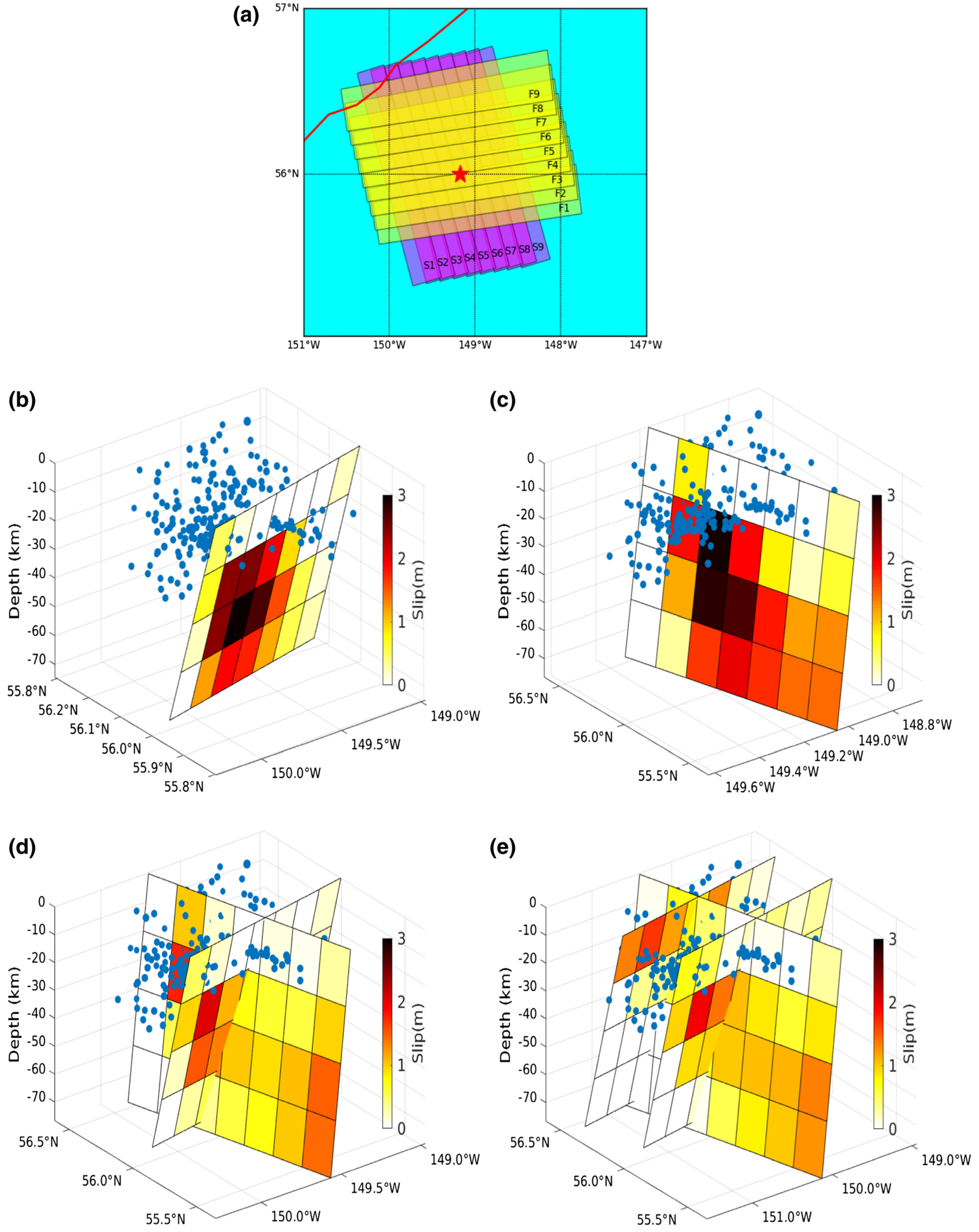
(a)
57°N
56°N
151°W
150°W
149°W
148°W
147°W
F9
F8
F7
F6
F5
F4
F3
F2
F1
S1 S2 S3 S4 S5 S6 S7 S8 S9
(b)
(c)
(d)
(e)
Depth (km)
0
-10
-20
-30
-40
-50
-60
-70
Slip(m)
0
1
2
3
55.8°N
56.2°N
56.1°N
56.0°N
55.9°N
55.8°N
149.0°W
149.5°W
150.0°W
56.5°N
56.0°N
55.5°N
148.8°W
149.0°W
149.2°W
149.4°W
149.6°W
151.0°W

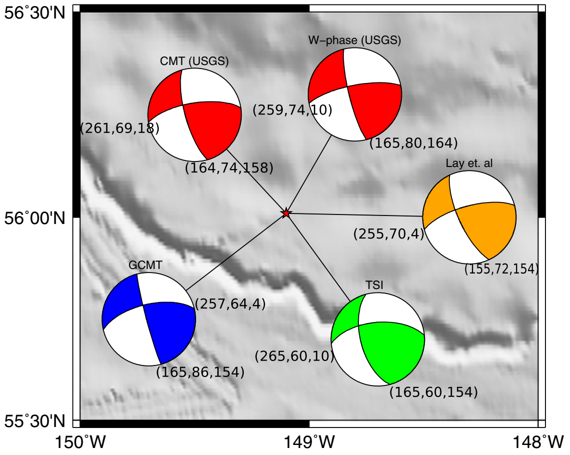

Figure 5
Focal mechanisms determined by USGS (red), GCMT (blue), and Lay et al. (2018) (orange). TSI (green) is our proposed focal mechanism, using the best fitting orientations of N–S and E–W planes

appropriate fault planes associated with the rupture process by searching over a grid of 18 faults with nine parallel fault planes spaced 10 km apart in each direction (N–S and E–W striking). The faults are denoted as $\{F_1, \ldots, F_9\}$ for faults with E–W strike and northward dip and $\{S_1, \ldots, S_9\}$ for faults striking N–S with westward dip (Fig. 4a). Among them, we chose the faults based on the smallest "residual error", defined as the l_2 norm of the difference between the SSD model (determined by inverting tsunami data) and the WSD model (calculated from the earthquake slip distribution) (Fig. 3).

Figure 7 ►
a Sea-floor deformation calculated from the slip distribution of our preferred three-fault model; **b** (dashed black) observed tsunami waveforms, (red) modeled waveforms from the tsunami SSD model (Fig. 2a), (green) modeled waveforms from the earthquake slip distribution (**a**). The first seven DART buoys are used in the inversion, other DART and tide gauge stations shown are for comparison

Initially, we use fault orientations from the USGS CMT solution (N–S and E–W oriented faults: strike $\psi_1 = 164°$, dip $\phi_1 = 74°$, rake $r_1 = 158°$ and strike $\psi_2 = 261°$, dip $\phi_2 = 69°$, rake $r_2 = 18°$). We approximate each fault using a 7×4 grid of sub-faults of dimension of $20 \times 20\,\text{km}^2$. Using these fault parameters with unit slip, we compute synthetic GFs of sea-floor deformation (different from tsunami GFs of section 4) for each sub-fault using the Okada (1985) model over the same domain as the SSD model. The domain extends from 54° N–58° N and 152° W–146° W (Fig. 2a) with grid spacing of 1 arc min, giving a total number of grid points of 87001 ($= 361 \times 241$). The sea-floor deformation is assumed to be identical to the sea-surface displacement. We store the GFs associated with each sub-fault in each column of the matrix G and the sea-surface displacement as the vector d that yields the system $Gm = d$. The length of each column of G is 87,001 and the number of columns depends on how many fault planes are considered in the source inversion.

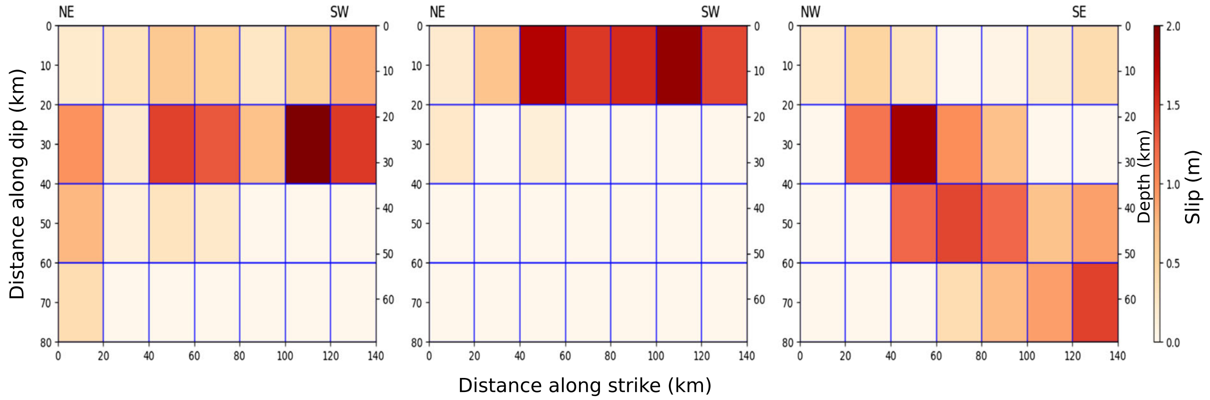

Figure 6
Slip distribution for the preferred model, which has three faults: F_4 (left), F_8 (middle), S_5 (right). Color represents amount of slip in each sub-fault

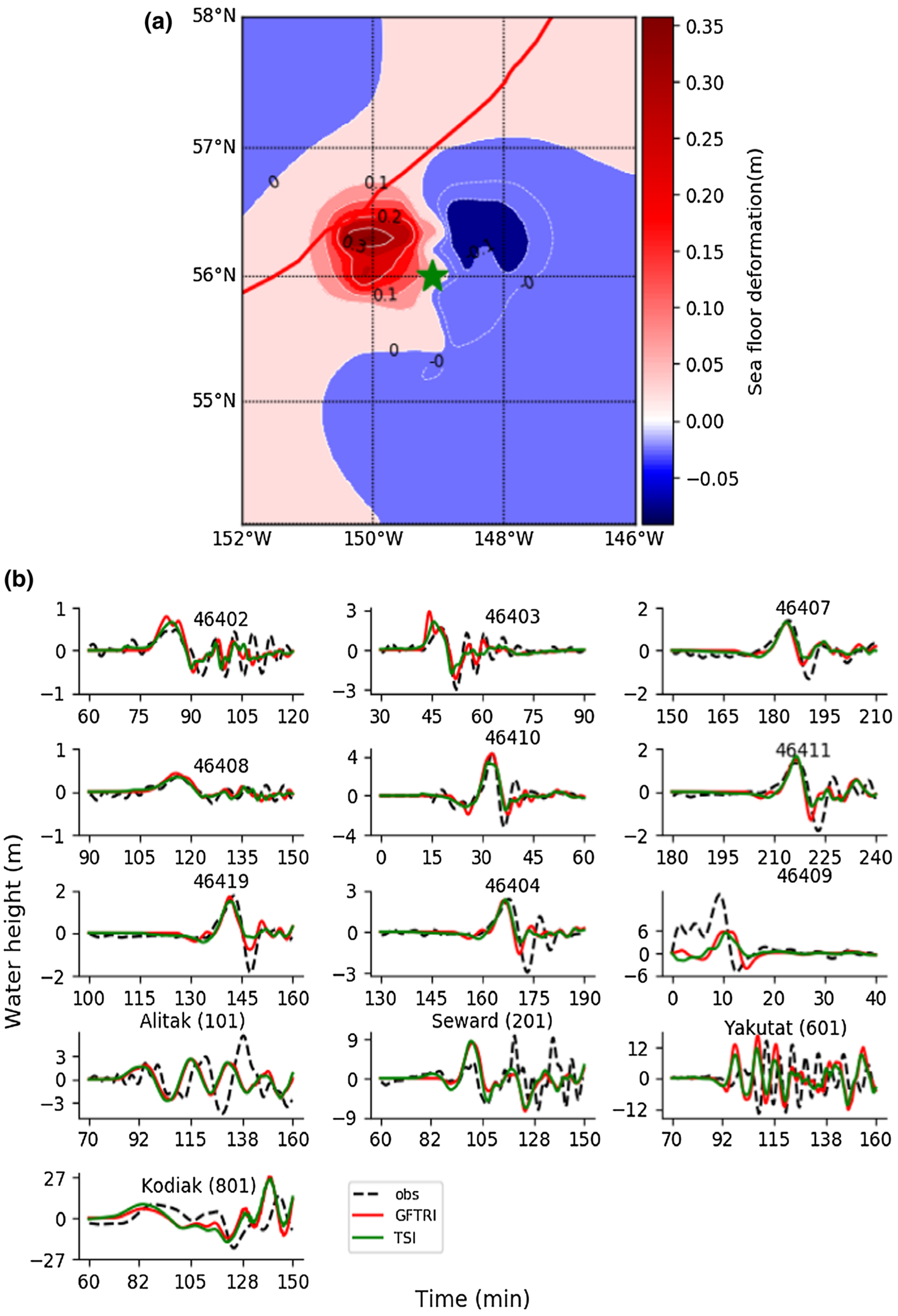

The vector m that we solve for represents the slip over the subfaults. The system is solved by using a non-negative least squares method with damping and smoothing constraints- (0.3 and 0.01, respectively) chosen by trial and error in order to obtain a stable solution.

We assume that the rupture is associated with several fault planes oriented in N–S and E–W directions, based on the aftershock locations and previous studies. To find the optimal combination of ruptured faults, we consider several scenarios: case 1) a single fault in either N–S or E–W orientation; case 2) two faults, with a fixed fault from case 1 (the case 1 fault that provides the smallest residual error); case 3) three faults, with two fixed faults determined in case 2; case 4) four faults, with three from case 3; case 5) five faults, with four fixed faults determined in case 4; and finally, case 6) six faults with five fixed faults from case 5.

In case 1, we carried out 18 earthquake slip inversions in total; nine for each direction (Fig. 3a, b). The inversion using fault F_4 in the E–W direction produces the smallest residual error and is thus fixed in the next case 2. In case 2, we fix fault F_4 in case 1 and search over the nine faults in the N–S direction and find that the combination of faults $F_4 \,\&\, S_5$ provides the smallest error (Fig. 3c). These two faults ($F_4 \,\&\, S_5$) are fixed for case 3, where we conducted 16 inversions with one of the remaining 8 faults in both E–W and N–S directions in each inversion. The residual error is presented in Fig. 3d, e; comparing the errors in different fault combinations, we find that the set of $\{F_4, F_8, S_5\}$ produces the smallest residual error. In case 4, we consider these three faults $F_4, F_8 \,\&\, S_5$ with one of the remaining 8 faults in the N–S direction and find that the error varies very slightly. In a similar way, we conducted inversion for the case of 5 and 6 using five and six faults; the resulting error variation is so subtle that it is difficult to distinguish which fault should be considered for improving the result. We concluded that the set of three faults $\{F_4, F_8, S_5\}$ in case 3 is sufficient for recovering the SSD model. The residual error is 0.396 and the slip distribution is displayed in Supplementary Figure S2. In our model the maximum slip occurs on E–W fault F_4 at a depth of 20 km. In this model, the total seismic moment is 9.37×10^{20} Nm, M_w7.9, which is very close to both the USGS and global CMT (GCMT) solution.

Our initial fault plane orientations were based on the USGS CMT solution. However, subsequent studies have suggested a range of possible solutions (Fig. 5 and references in caption). Thus, we perturbed the strike, dip, and rake of the 3 planes of our preferred model (case 3) within a range consistent with the previous studies of Lay et al. (2018), USGS and GCMT. We varied the strike in 5° increments from 150° to 175° for the N–S-striking planes and from 250° to 275° for the E–W striking planes; the dip was varied in 5° increments from 60° to 85° for both westward and northward dipping planes. We varied the rake in 3° increments from 154° to 163° for the N–S-striking and from 10° to 19° for the E–W striking planes. With these variations, we inverted the SSD model for earthquake slip model and found the smallest residual error (misfit) between the SSD model and the WSD model resulted from the parameters (strike, dip, rake): (165°, 60°, 154°) and (265°, 60°, 10°) for the N–S and E–W striking planes, respectively (Fig. 5). We found that the smallest value of the rake in the range was preferred for both planes whereas strike and dip changed by a smaller amount. The slip distribution over the faults with this set of parameters is displayed in Fig. 6 and the WSD model is presented in Fig. 7a.

6. *Discussion*

After performing our two step inversions (TSI), which first consists of Green's function based time reverse imaging (GFTRI) for the sea surface displacement (SSD) model (Sect. 4), followed by inversion of the SSD model for the fault model (earthquake slip distribution) (Sect. 5), we find a preferred fault model consisting of one N–S oriented fault and two E–W oriented faults (Fig. 6). The coseismic water surface displacement (WSD) model from our preferred earthquake fault model can reproduce the peak of the observed waveform, but not the trough in the leading wave, particularly at stations 46411 and 46419 in Fig. 7b. This misfit indicates that the WSD model cannot recover subsidence of the sea surface completely. On the other hand, our SSD model can explain the observed tsunami waveforms very well at most DART stations including DART station 46404 which is not used in the source inversion (Fig. 7b). DART 46409 is in close proximity to the source and is not well fit. Lay et al. (2018) also modeled lower water height than the observed at station 46409. We believe that the observed wave height at station 46409 may be a combination of the tsunami wave and the seismic wave, such as the Rayleigh wave as it is located very near to the epicenter. In addition, the fit at tide gauges (not used in source inversion) is not as good as the fit at the DART stations. This could be due to in part to the insufficient grid resolution (20/3 arc sec) used in coastal regions for the tsunami simulation.

From the SSD model we determine the multi-fault earthquake slip distribution model by using the TSI method (Sect. 5). In total, 18 faults were considered in both approximately N–S and E–W directions. Our preferred fault model consists of three faults with slip distribution on the E–W oriented faults located in a spatially compact region shallower than 40 km. On the southernmost E–W fault F_4, the major slip is located within the depth range 18 km to 35 km and on F_8, the major slip is shallower than 20 km. In contrast, the slip on the N–S oriented fault is distributed over a wider range of depths, with the major slip at 20–60 km depth.

Our results, obtained from GFTRI of tsunami data, are broadly consistent with the results obtained in other studies which used seismic, GPS, and in some cases tsunami data. The details between the previous studies vary, including the number of faults, the orientation of the segment which released the most energy (NE-SW trending left-lateral strike-slip segments (Ruppert et al. 2018; Zhao et al. 2018), or right-lateral slip on SSE-trending fault Lay et al. (2018). Nevertheless, all studies require faulting on a set of conjugate faults roughly oriented N–S and E–W. (Krabbenhoeft et al. 2018) included analysis of gravity, magnetics, and bathymetry data of the outer-rise of the Alaska subduction zone in their study of the Kodiak event. They find a N–S aligned crustal fabric influenced by plate bending normal faults, N–S magnetic anomalies, and E–W oriented fracture zones.

7. Conclusion

We estimated the tsunami source model (sea surface displacement model or SSD) of the 2018 offshore Kodiak earthquake tsunami by utilizing the Green's function based time reverse imaging (GFTRI) method. The SSD model determined using tsunami data from the seven DART stations provides good waveform fits between observed and simulated waveforms, the period of the tsunami arrival matches well, and the peak amplitudes are compatible with the observed waveforms. We used DART stations located around the source in the Gulf of Alaska and North Pacific Ocean. The performance could possibly be improved by adding far-field stations located in the Pacific Ocean, which would improve the azimuthal coverage though perhaps at the expense of signal to noise ratio.

We inverted the SSD model for the earthquake slip distribution over a range of fault combinations chosen in a systematic manner. Our preferred fault model consists of three faults. We perturbed the fault parameters using bounds from previously published work to further determine optimal fault orientations. Our preferred earthquake slip model produces sea-surface uplift (water surface displacement or WSD) well-matched with the SSD model. Overall, the WSD model from the three fault model is consistent with the SSD model although it is unable to recover the subsidence completely. While seismic and GPS data are of enormous utility and provide important information, we find that with the computationally efficient two-step inversion (TSI) method, which only needs tsunami data as input, we can recover the major aspects of the tsunami source and earthquake source associated with the 2018 offshore Kodiak earthquake.

Acknowledgements

This work utilized the RMACC Summit supercomputer, which is supported by the National Science Foundation (awards ACI-1532235 and ACI-1532236), the University of Colorado Boulder, and Colorado State University. The Summit supercomputer is a joint effort of these two universities. We thank Aaron Sweeney (NOAA) for checking Kodiak tide gauge data, Dmitry Nicolsky (University of Alaska) & Nicolas Arcos (NOAA) for providing bathymetry data covering the Alaska region and Leonardo Ramirez-Guzman (National Autonomous University of Mexico) for providing a MATLAB script for 3D plot. The first author thanks the Cooperative Institute for

Research in Environmental Sciences (CIRES) for supporting this research through a postdoctoral visiting fellowship. This work was supported in part by NSF Award Number ICER 1855090.

REFERENCES

An, C., Sepúlveda, I., & Liu, P. L. F. (2014). Tsunami source and its validation of the 2014 Iquique, Chile, earthquake. *Geophysical Research Letters*, *41*(11), 3988–3994.

Baba, T., Allgeyer, S., Hossen, M. J., Cummins, P. R., Tsushima, H., Imai, K., et al. (2017). Accurate numerical simulation of the far-field tsunami caused by the 2011 Tohoku earthquake, including the effects of Boussinesq dispersion, seawater density stratification, elastic loading, and gravitational potential change. *Ocean Modelling*, *111*, 46–54. https://doi.org/10.1016/j.ocemod.2017.01.002.

Baba, T., & Cummins, P. R. (2005). Contiguous rupture areas of two Nankai Trough earthquakes revealed by high-resolution tsunami waveform inversion. *Geophysical Research Letters*, *32*(8), L08305. https://doi.org/10.1029/2004GL022320.

Gusman, A. R., Mulia, I. E., & Satake, K. (2018). Optimum sea surface displacement and fault slip distribution of the 2017 Tehuantepec earthquake (Mw 8.2) in Mexico estimated from tsunami waveforms. *Geophysical Research Letters*, *45*(2), 646–653.

Gusman, A. R., Mulia, I. E., Satake, K., Watada, S., Heidarzadeh, M., & Sheehan, A. F. (2016). Estimate of tsunami source using optimized unit sources and including dispersion effects during tsunami propagation: The 2012 Haida Gwaii earthquake. *Geophysical Research Letters*, *43*(18), 9819–9828.

Ho, T. C., Satake, K., & Watada, S. (2017). Improved phase corrections for transoceanic tsunami data in spatial and temporal source estimation: Application to the 2011 Tohoku Earthquake. *Journal of Geophysical Research: Solid Earth*, *122*(12), 10–155.

Hossen, M. J., Cummins, P. R., Dettmer, J., & Baba, T. (2015a). Time reverse imaging for far-field tsunami forecasting: 2011 Tohoku earthquake case study. *Geophysical Research Letters*, *42*(22), 9906–9915.

Hossen, M. J., Cummins, P. R., Dettmer, J., & Baba, T. (2015b). Tsunami waveform inversion for sea surface displacement following the 2011 Tohoku earthquake: Importance of dispersion and source kinematics. *Journal of Geophysical Research: Solid Earth*, *120*(9), 6452–6473.

Hossen, M. J., Cummins, P. R., Roberts, S. G., & Allgeyer, S. (2015c). Time reversal imaging of the tsunami source. *Pure and Applied Geophysics*, *172*(3–4), 969–984.

Hossen, M. J., Gusman, A., Satake, K., & Cummins, P. R. (2018). An adjoint sensitivity method applied to time reverse imaging of tsunami source for the 2009 Samoa earthquake. *Geophysical Research Letters*, *45*(2), 627–636.

Korolev, Y. P. (2011). An approximate method of short-term tsunami forecast and the hindcasting of some recent events. *Natural Hazards and Earth System Sciences*, *11*(11), 3081–3091. https://doi.org/10.5194/nhess-11-3081-2011. https://www.nat-hazards-earth-syst-sci.net/11/3081/2011/.

Krabbenhoeft, A., von Huene, R., Miller, J. J., Lange, D., & Vera, F. (2018). Strike-slip 23 January 2018 MW 7.9 Gulf of Alaska rare intraplate earthquake: Complex rupture of a fracture zone system. *Scientific Reports*, *8*(1), 13706.

Lay, T., Ye, L., Bai, Y., Cheung, K. F., & Kanamori, H. (2018). The 2018 MW 7.9 Gulf of Alaska earthquake: Multiple fault rupture in the Pacific plate. *Geophysical Research Letters*, *45*(18), 9542–9551.

Mulia, I. E., & Asano, T. (2016). Initial tsunami source estimation by inversion with an intelligent selection of model parameters and time delays. *Journal of Geophysical Research: Oceans*, *121*(1), 441–456.

Mulia, I. E., Gusman, A. R., Jakir, Hossen M., & Satake, K. (2018). Adaptive tsunami source inversion using optimizations and the reciprocity principle. *Journal of Geophysical Research: Solid Earth*, *123*(12), 10–749.

Mungov, G., Eblé, M., & Bouchard, R. (2013). DART® tsunameter retrospective and real-time data: A reflection on 10 years of processing in support of tsunami research and operations. *Pure and Applied Geophysics*, *170*(9–10), 1369–1384.

Okada, Y. (1985). Surface deformation due to shear and tensile faults in a half-space. *Bulletin of the Seismological Society of America*, *75*(4), 1135–1154.

Ruppert, N., Rollins, C., Zhang, A., Meng, L., Holtkamp, S., West, M., et al. (2018). Complex faulting and triggered rupture during the 2018 MW 7.9 offshore Kodiak, Alaska, earthquake. *Geophysical Research Letters*, *45*(15), 7533–7541.

Satake, K. (1987). Inversion of tsunami waveforms for the estimation of a fault heterogeneity: Method and numerical experiments. *Journal of Physics of the Earth*, *35*(3), 241–254.

Satake, K., Fujii, Y., Harada, T., & Namegaya, Y. (2013). Time and space distribution of coseismic slip of the 2011 Tohoku earthquake as inferred from tsunami waveform data. *Bulletin of the Seismological Society of America*, *103*(2B), 1473–1492.

Weatherall, P., Marks, K. M., Jakobsson, M., Schmitt, T., Tani, S., Arndt, J. E., et al. (2015). A new digital bathymetric model of the world's oceans. *Earth and Space Science*, *2*(8), 331–345.

Wei, Y., Cheung, K. F., Curtis, G. D., & McCreery, C. S. (2003). Inverse algorithm for tsunami forecasts. *Journal of Waterway, Port, Coastal, and Ocean Engineering*, *129*(2), 60–69.

Yue, H., Lay, T., & Koper, K. D. (2012). En échelon and orthogonal fault ruptures of the 11 April 2012 great intraplate earthquakes. *Nature*, *490*(7419), 245.

Zhao, B., Qi, Y., Wang, D., Yu, J., Li, Q., & Zhang, C. (2018). Coseismic slip model of the 2018 M w 7.9 Gulf of Alaska earthquake and its seismic hazard implications. *Seismological Research Letters*, *90*(2A), 642–648.

(Received August 14, 2019, revised January 24, 2020, accepted January 28, 2020, Published online February 5, 2020)